Version 2.0 July 14, 1998

Submitted to the 29th International Conference on High-Energy Physics ICHEP98,
Vancouver, Canada, July 1998

Measurement of Di-jet Cross-Sections in Low Q^2 Deep-Inelastic Scattering Processes at HERA and Extraction of an Effective Parton Density of the Virtual Photon

H1 Collaboration

Abstract

The triple-differential dijet cross section, $\mathrm{d}^3\sigma_{ep}/\mathrm{d}Q^2\mathrm{d}\overline{E_t}^2\mathrm{d}x_\gamma^{jets}$, is measured in deep-inelastic scattering processes for photon virtuality $1.6 < Q^2 < 80$ GeV^2 with the H1 detector at HERA. The results are compared with leading order QCD models which include the effects of a resolved component to the virtual photon. An effective leading order parton density for the virtual photon is extracted as a function of the photon virtuality, the probing scale and the parton momentum fraction. A logarithmic scale dependence and a suppression with increasing Q^2 is seen. The parton densities are compared with QCD inspired parameterisations.

Abstract 544 : Parallel 5,3, Plenary 7,5 **Abstract: 544**
Parallel sessions: 5,3
Plenary sessions: 7,5

1 Introduction and Motivation

It has been well-established that the real photon has an hadronic structure both through measurements of the photon structure in two-photon collisions at electron-positron colliders [1] and measurements of the photoproduction of jets at HERA [2]. The data have been used to determine universal parton densities for real photons. The behaviour of this hadronic structure as the photon becomes virtual is of great interest [3] because it provides a universal QCD framework with which to link deep-inelastic ep collisions, photoproduction and two-photon processes. Experimental data with virtual target photons in two-photon collisions is, however, sparse [4]. The ep collision data at HERA on the other hand is available over a wide range of photon virtualities, Q^2, from photoproduction to high-Q^2 deep inelastic scattering and is also sensitive to photon structure [5, 6, 7].

The production of high transverse momentum (P_t) jets in ep collisions at $Q^2 \ll M_Z^2$, where M_Z is the Z-boson mass, is dominated by processes in which a single space-like virtual photon carries the momentum transfer from the electron. When this photon is quasi-real, i.e. in photoproduction processes, two types of interaction can be distinguished in leading order: direct processes in which the photon couples as a pointlike object to a parton out of the proton and resolved processes in which it develops an hadronic structure prior to the collision. In the latter case, a parton out of the photon, carrying only a fraction x_γ of the photon's momentum, enters the hard scattering. The photoproduction jet cross-section is therefore sensitive to the density of partons in the photon and the latter can be measured. The scale at which this photon structure is probed is determined by the P_t of the jets.

When the exchanged photon is highly virtual, the production of high-P_t jets is usually interpreted as deep-inelastic scattering (DIS). Here the photon interacts only as a point-like object, or, in the terminology of photoproduction, the interaction is purely direct. However, as long as the photon is probed with sufficiently high resolution, i.e. if $P_t^2 \gg Q^2$, it is still possible to have interactions in which its structure is resolved. It is a prediction of perturbative QCD that the parton densities of virtual photons become suppressed as Q^2 increases [5, 7, 8, 9, 10] and that the hadronic structure in the photon becomes simpler, eventually reducing to purely direct coupling to a $\mathrm{q\overline{q}}$ pair. The concept of virtual photon structure thus provides a unified description of high P_t jet production over the whole range of Q^2 and a smooth transition between photoproduction and DIS processes.

In a previous publication [11], it was shown that the single inclusive jet cross-section in photoproduction and low Q^2 deep-inelastic scattering can indeed be described by models which include a contribution from resolved virtual photons which is suppressed with increasing Q^2.

With dijet events, it becomes possible to reconstruct the variable x_γ which, in leading order, can be interpreted as the momentum fraction of the parton out of the photon entering into the hard scattering process. Although the initial state quarks and gluons in the hard scattering process cannot be distinguished, an effective parton density [12], a linear combination of quark and gluon densities of the photon, can be determined. This measurement has been made for quasi-real photons using photoproduction events [13] and has been shown to exhibit the logarithmic scaling violations that are characteristic of photon structure. More recently, the dijet cross-section has been measured in low-Q^2 deep-inelastic scattering processes and has been found to be best described when the effects of virtual photon structure are included in predictions [14].

In this paper we extend these studies by measuring dijet cross-sections in low-Q^2 deep inelastic scattering events and investigate the evolution of the effective parton density with Q^2

as well as the P_t^2 of the partons. We begin by measuring the triple-differential jet cross-section, $\mathrm{d}^3\sigma_{ep}/\mathrm{d}Q^2\mathrm{d}\overline{E_t}^2\mathrm{d}x_\gamma^{jets}$, where $\overline{E_t}$ is the mean of the transverse energies of the two highest E_t jets measured in the $\gamma^* p$ centre of momentum frame, x_γ^{jets} is the value of x_γ as estimated from the jets and Q^2 is the virtuality of the exchanged photon. Jets were found using the inclusive k_T algorithm [15]. The measured cross-section is compared to LO simulations which include models for the virtual photon structure.

The measured cross-section is then used to extract a leading order effective parton density as a function of x_γ, Q^2 and P_t^2. The observed shape, scaling behaviour and virtuality dependence of this effective parton density is compared with various parameterisations based on predictions from perturbative QCD.

2 The H1 Detector

The H1 detector is described in detail in [16]. In this analysis, we make particular use of the SPACAL [17] calorimeter for detection and identification of the scattered positron. The hadronic energy flow is measured with the Liquid Argon [18] (LAr) and SPACAL calorimeters. The central and forward tracking detectors are used to reconstruct the event vertex and to supplement the measurement of hadronic energy flow made by the LAr and SPACAL.

We use a coordinate system in which the nominal interaction point is at the origin and the incident proton beam defines the $+z$ direction. The polar angle θ is defined with respect to the proton direction.

The central tracking system consists of two concentric cylindrical drift chambers, coaxial with the beamline and centered about the nominal interaction vertex. Its polar angle coverage, $20^\circ < \theta < 165^\circ$, is complemented by that of the forward tracker, $7^\circ < \theta < 20^\circ$. The central tracker is interleaved with drift chambers providing measurement of the z coordinates of the tracks. The tracking detectors are immersed in a 1.15 T magnetic field generated by a superconducting solenoid which surrounds the LAr. The LAr is a finely grained calorimeter covering the range in polar angle $4^\circ < \theta < 154^\circ$ with full azimuthal acceptance. It consists of an electromagnetic section with lead absorbers, 20–30 radiation lengths in depth, and an hadronic section with steel absorbers. The total depth of the calorimeter varies between 4.5 and 8 hadronic interaction lengths. The energy resolution is $\sigma(E)/E \approx 0.12/\sqrt{E}$ for electrons and $\sigma(E)/E \approx 0.5/\sqrt{E}$ for pions (E in GeV), as measured in test beams [19]. The absolute energy scale is known to a precision of 3% for electrons and 4% for hadrons. The SPACAL is a lead/scintillating-fibre calorimeter covering the angular region $153^\circ < \theta < 177.8^\circ$. It contains electromagnetic and hadronic sections. The former has an energy resolution of $7.5\%/\sqrt{E} \oplus 2.5\%$. The SPACAL provides the main trigger for the events (see section 4) in this analysis. Timing resolution of better than 1 ns in both sections of the calorimeter is exploited in the trigger to reduce proton beam induced background. The energy scale uncertainty of the hadronic section is 7%. The backward drift chamber (BDC) system in front of the SPACAL spanning the region $151^\circ < \theta < 177.5^\circ$ provides track segment information to augment positron identification in the SPACAL and, in conjunction with the event vertex determination from the central and forward track detectors, gives a precision measurement of the positron scattering angle.

The luminosity determination is based on measurement of $\mathrm{ep} \to \mathrm{ep}\gamma$ processes. The electron and photon are detected in the electron tagger located at $z = -33.4$ m and photon tagger at $z = -103$ m, respectively. Both consist of crystal Cherenkov calorimeters with a resolution of $\sigma(E)/E \approx 0.1\sqrt{E}$. The integrated luminosity was measured to a precision of better than 2%.

3 Theoretical Models and Simulations

The analysis uses simulated events both to correct the measured cross-sections for detector effects and in order to compare the data with the predictions of various theoretical models.

The HERWIG [20] and RAPGAP [21] Monte Carlos are both able to simulate the direct and resolved production of dijets by virtual photons. In both models the hard scattering process is simulated in leading order (LO) regulated with a minimum P_t cut off, P_t^{min}, and supplemented by initial and final state parton showers. In the simulation of resolved processes, the equivalent photon approximation is used for the transverse photon flux. The longitudinal flux is not included. Exact $\mathrm{eq} \rightarrow \mathrm{eqg}$ and $\mathrm{eg} \rightarrow \mathrm{eq\overline{q}}$ matrix elements are used for the direct component. HERWIG uses exact, noncollinear kinematics at the electron vertex.

HERWIG has parton showering based on colour coherence [22] and uses the cluster model for hadronisation. Some tuning of the parton showering is possible and we use two different settings (specified by the parameter QSPAC) in the analysis. In addition to the hard scattering process, HERWIG can also model remnant-remnant interactions in the form of a soft underlying event. These result in a flow of transverse energy uncorrelated with the hard scattering process but contributing to the flow of energy in and around the jets. The probability that a resolved event contains soft underlying activity can be adjusted in the simulation.

RAPGAP uses the LUND string model [23] for hadronisation and contains no mechanism for simulating multiple parton interactions.

The factorisation scales of the proton and photon parton densities were both set equal to the P_t of the scattered partons. The simulations have interfaces to a variety of parameterisations of photon and proton parton density functions. GRV parton densities were used for the proton [24]. Several models for the virtual photon parton densities were considered.

The Drees-Godbole model [9, 10] starts with real photon parton densities [25] and suppresses them by a factor, $\mathcal{L}$, which depends on Q^2, P_t^2 and a free parameter, ω:

$$\mathcal{L}(Q^2, P_t^2, \omega^2) = \frac{\ln((P_t^2 + \omega^2)/(Q^2 + \omega^2))}{\ln((P_t^2 + \omega^2)/\omega^2)} \tag{1}$$

Quark densities in the real photon are suppressed by $\mathcal{L}$ and the gluon densities by $\mathcal{L}^2$. This ansatz, based on the analysis in [10], is designed to interpolate smoothly between the leading-logarithmic part of the real photon parton densities, $\sim \ln(P_t^2/\Lambda_{QCD}^2)$ and the asymptotic domain, $P_t^2 \gg Q^2 \gg \Lambda_{QCD}^2$, where the photon density functions are predicted by perturbative QCD to behave as $\sim \ln(P_t^2/Q^2)$. The shape of the x_γ distribution evolves with Q^2 because of the different suppression of the quark and gluon densities. We find that ω values $\sim 0.1 - 0.2$ GeV lead to reasonable descriptions of the data used in this analysis.

In the models of Schuler and Sjöstrand [26], the virtual photon parton densities are decomposed into a non-perturbative component modelled by vector meson dominance (VMD) and a perturbative anomalous component. As Q^2 increases, the VMD component is rapidly suppressed, $\sim (m_V^2/(m_V^2 + Q^2))^2$, whereas the anomalous part has a slower logarithmic suppression and is again designed to approach the exact QCD predictions in the $P_t^2 \gg Q^2 \gg \Lambda_{QCD}^2$ region.

The various combinations of Monte Carlo simulations and parton densities used in the analysis are summarised in Table 1.

Model name	α_s	P pdf	γ^* pdf	$\mathrm{P_t^{min}}$	SUE	Other
HERWIG(HO)/DG	2-loop	GRV-HO	GRV-HO*DG ($\omega = 0.2$)	3	10%	QSPAC=1.0
RAPGAP(HO)/SAS-2D	1-loop	GRV-HO	SAS-2D	3	-	-
HERWIG(LO)/DG	1-loop	GRV-LO	GRV-LO*DG ($\omega = 0.2$)	2	5%	QSPAC=2.0
RAPGAP(LO)/DG	1-loop	GRV-LO	GRV-LO*DG ($\omega = 0.2$)	2	-	-
RAPGAP(LO)/SAS-2D	1-loop	GRV-LO	SAS-2D	2	-	-
RAPGAP(LO)/SAS-1D	1-loop	GRV-LO	SAS-1D	2	-	-

Table 1: Description of models. The first two models are used to correct for detector effects. The remainder are used in the unfolding of the diparton cross-section from the corrected jet cross-section and for comparison with the corrected cross-section and effective parton density.

4 Event Selection

The analysis is based on positron-proton collision data collected by the H1 detector at HERA in 1996 and corresponds to an integrated luminosity of 6 pb^{-1}. The events were triggered by an energy cluster exceeding a threshold energy in the electromagnetic section of the SPACAL of $> 2.5(5.7)$ GeV at large (small) radii provided this was accompanied by at least one track in the central tracking device with momentum > 800 MeV and a well defined interaction vertex. Time-of-flight information was used to veto out-of-time events. The efficiency of this trigger is typically $\sim 90\%$ and has been measured over the relevant kinematic range to a precision of 5%.

Additional criteria were then applied to reduce backgrounds and ensure that the events were well-measured. The energy cluster in the SPACAL was required to be consistent with being produced by an electron and to be well-contained. The reconstructed event vertex was required to lie within 30 cm of its nominal location in z. In order to further reduce photoproduction background, we required that $\sum_i (E^i - P_z^i)$, equal to $2E_e$ for DIS events, lie in the range 40–65 GeV. The sum is taken over calorimeter clusters supplemented by tracking information. The inelasticity, calculated from the energy, E_e', and polar angle, θ', of the scattered electron:

$$y_e \approx 1 - E_e'/E_e \sin^2(\theta'/2), \tag{2}$$

was restricted to the range $0.1 < y_e < 0.7$. The upper limit corresponds to a minimum scattered electron energy of ~ 8 GeV. Small y_e values, where the y_e resolution deteriorates, were excluded. The electron kinematics were also used to calculate the virtuality, Q^2, of the photon:

$$Q^2 \approx 4E_e' E_e \cos^2(\theta'/2), \tag{3}$$

The inclusive k_t-algorithm [15] was applied to find jets in the $\gamma^* p$ cms frame with the boost defined by the scattered electron kinematics. The clustering of final state objects into jets uses:

$$d_{ij} = \min(P_t^{i\,2}, P_t^{j\,2})\Delta R \tag{4}$$

$$\text{where} \qquad \Delta R = \sqrt{(\eta^i - \eta^j)^2 + (\phi^i - \phi^j)^2} \tag{5}$$

$$\text{and} \qquad d_i = P_t^{i\,2} \tag{6}$$

as the distance measures between objects i and j and between the i'th object and the beam respectively. The P_t^i, η^i and ϕ^i are the transverse momenta, pseudorapidities given by $\eta^i =$

$-\ln\tan(\theta^i/2)$ and azimuthal angles of the objects, respectively. At each iteration of the algorithm, the smallest distance measure is determined. If this is one of the d_{ij}, then the objects i and j are combined by addition of their 4-momenta. Whenever a d_i is the smallest distance measure, the i'th object defines a completed jet and is excluded from further iterations. The iterations terminate when all objects have been assigned to jets.

Events were required to contain at least two jets found by the above algorithm. Events were accepted if the two highest E_t jets (jet 1, jet 2) in the event satisfied the following criteria:

$$|(\eta^{jet\,1} - \eta^{jet\,2})| < 1.0 \tag{7}$$

$$-3.0 < \overline{\eta} < -0.5 \tag{8}$$

$$\overline{E}_t^2 > 30\ \mathrm{GeV}^2 \tag{9}$$

$$\frac{|(E_t^{jet\,1} - E_t^{jet\,2})|}{(E_t^{jet\,1} + E_t^{jet\,2})} < 0.25 \tag{10}$$

where $\overline{\eta}$ and $\overline{E}_t$ are the mean pseudorapidity and mean transverse energy of the two highest E_t jets. E_t and η are always given with reference to the $\gamma^* p$ cms. These cuts ensure that the jets are confined to a region of the detector where they are well-measured and that x_γ is well-determined. The constraints on E_t are such that the highest (second highest) E_t jet has $E_t \geq 7(4)$ GeV. After application of these selection criteria we obtained a sample of ~ 12000 dijet events with $\overline{E}_t^2 > 30\ \mathrm{GeV}^2$ spanning the Q^2 range $1.6 < Q^2 < 80\ \mathrm{GeV}^2$.

5 Measurement of the Triple Differential Di-jet Cross-section

We first study the dependence of the dijet cross-section on the variables x_γ, $\overline{E}_T$ and Q^2.

In each event, an estimate of x_γ was made using the energies and longitudinal momenta of the two highest E_T jets:

$$x_\gamma^{rec} = \frac{\sum\limits_{jet\ 1, jet\ 2} (E^{jet} - p_z^{jet})}{\sum\limits_h (E^h - p_z^h)}. \tag{11}$$

The sum in the denominator is over all reconstructed objects in the event (calorimeter clusters supported by tracking information) except for those associated with the scattered positron.

The measured dijet cross-sections were corrected for detector acceptance and resolution effects in separate ranges of reconstructed Q^2 by applying an iterative two-dimensional Bayesian unfolding technique [27] to distributions of x_γ^{rec} and $\overline{E}_T^{rec}$. The correlations between the measured variables $\{x_\gamma^{rec}, \overline{E}_T^{rec}\}$ and the corrected variables $\{x_\gamma^{jets}, \overline{E}_T\}$ were obtained using events generated by the HERWIG(HO)/DG model (see Table 1). The average resolutions were 0.13 for x_γ^{jets}, and 0.8 GeV^2 for Q^2. The resolution in $\overline{E}_t$ is $\sim 8\%$ in the highest $\overline{E}_t^2$ range reducing to $\sim 20\%$ in the lowest. The generated events were subjected to a detailed simulation of the H1 detector. A bin-by-bin correction was then applied for the Q^2 dependence for which the measurement error is much smaller than the bin size and migrations are negligible. After unfolding, the correlated error between bins in the unfolded distributions was $< 40\%$. By varying the number of iterations used, we estimated that unfolding instabilities result in a 5% systematic uncertainty in the unfolded cross-sections which we include in the systematic errors.

The unfolding procedure might be influenced by several model-dependent factors including the soft underlying event. In figure 1 we show the measured transverse energy flow in ϕ in a strip of ± 1 unit of pseudorapidity about the axes of the two highest E_t jets in the events for different ranges of jet E_T and η. Because the two jets are constrained to be close together in η, the energy flow associated with the other jet is clearly visible. The flow produced by the other jet is dependent on event topology as well as the jet properties. We therefore exploit the fact that the jets are not precisely back-to-back in ϕ and orient the flow so that axis of the other high E_t jet is to the left exposing a wider pedestal region to the right. The flow is compared with the HERWIG(HO)/DG simulation with 10% soft-underlying event and with predictions from RAPGAP(HO)/SAS-2D which includes no model for the soft underlying event. Both simulations give a good description of the energy flow in the core of the jets. Neither model is able to describe the energy flow in the pedestal region in all ranges of E_t and η. For $\eta < -2.0$, the pedestal is well described by RAPGAP. In the forward region, $\eta > -1.25$, the data lies between the RAPGAP and HERWIG predictions. Although HERWIG overestimates the data in this inclusive plot, we find that 10% soft underlying event is needed to account for the pedestal observed for $Q^2 \lesssim 8$ GeV (not shown separately). The unfolding was repeated using HERWIG(HO)/DG with 0% and 15% soft underlying event. Differences in the resulting distributions were found to be everywhere $< 2\%$ and are included in the systematic errors.

Model dependencies from the choice of parton showering and hadronisation models and photon parton densities are together responsible for the largest systematic errors These were estimated by unfolding with the RAPGAP(HO)/SAS-2D simulation and result in a $\sim$ 17% systematic effect.

Uncertainties of 4% and 7% in the Liquid Argon and SPACAL calorimeter hadronic energy scales lead to 10% and 1% systematic errors in the results, respectively. There is a 2% uncertainty in the SPACAL electromagnetic energy scale which yields a 4% systematic effect and an additional 0.5% arises from an uncertainty of 1 mrad in the measurement of the electron scattering angle. The trigger efficiency uncertainty results in a 7% error. Radiative corrections result in a change in the cross-sections which is everywhere less than 10%. The data are not corrected for this. The residual background from photoproduction is negligible.

The corrected triple differential cross-section is shown in figures 2 , 3 and 4 as functions of x_γ^{jets}, $\overline{E_t}^2$ and Q^2 respectively. In each case, the distributions are shown for ranges of the other two variables. The data are depicted as points with error bars. Inner error bars show the statistical errors and the outer errors show the statistical and systematic errors added in quadrature. The absence of a data point indicates that no measurement was made in that bin.

In figure 2, the x_γ^{jets} distributions can be seen to peak towards $x_\gamma^{jets} = 1$, where the direct photon contribution is expected to be concentrated. The decrease in the cross-section in the lowest x_γ^{jets} bin arises from the cut in $\overline{\eta}$. There is a strong decrease in the cross-section with increasing $\overline{E_t}^2$. The relative contribution from resolved photons, in the region $x_\gamma^{jets} \lesssim 0.75$, diminishes as Q^2 increases at fixed $\overline{E_t}^2$. The data are compared with the HERWIG(LO)/DG simulation for two choices of the Q^2 suppression factor, ω. The predictions for the direct only contribution are also shown. With $\omega = 0.1$, the HERWIG(LO)/DG model gives a good description of the cross-section throughout the Q^2-$\overline{E_t}^2$ range. Increasing ω to 0.2 leads to an overestimation in the low Q^2, low $\overline{E_t}^2$ regions. However, it should be noted that changing the amount of soft underlying event changes the value of ω which best describes the data. The RAPGAP(LO)/DG model prediction (not shown in this figure), which contains no soft underlying event, requires $\omega \sim 0.2$ in order to describe the data. The direct only contribution is able to describe the data in the highest x_γ^{jets} bin at all Q^2 and $\overline{E_t}^2$ but underestimates the data for $x_\gamma^{jets} \lesssim 0.75$ except possibly in the highest Q^2, lower $\overline{E_t}^2$ ranges where $Q^2 \sim \overline{E_t}^2$.

Figure 3 compares the $\overline{E_t}^2$ dependence of the cross-section with predictions from RAPGAP(LO) with three different choices for the photon parton densities. The RAPGAP(LO)/DG model is shown as the full curve. RAPGAP(LO)/SAS-1D and RAPGAP(LO)/SAS-2D are shown as the dashed and dot-dashed curves, respectively. In the highest x_γ^{jets} range, where direct processes are expected to dominate, all the models give a good description of the data. Elsewhere, the models provide a spread of predictions but there is no single preferred model. The Drees-Godbole model tends to overestimate the cross section for $1.6 < Q^2 < 3.5\ \mathrm{GeV}^2$. For $Q^2 > 3.5\ \mathrm{GeV}^2$ and $0.45 < x_\gamma < 0.75$, all three models underestimate the data but are still compatible within errors.

The Q^2 dependence of the cross-section is shown in figure 4. There is a steep decrease in the cross-section with Q^2. The rate of decrease becomes smaller as x_γ^{jets} increases and is well-described by the RAPGAP(LO)/DG model shown as the full curve. The expectation from the direct-only component of RAPGAP, shown as the dashed curve, predicts a rate of suppression of the cross-section which is lower than that seen in the data except for $x_\gamma^{jets} > 0.75$ where the point-like processes dominate the cross-section. This is indicative of additional suppression arising from the photon parton densities.

From the above comparisons we can conclude that the observed dependence of the triple-differential dijet cross-section is consistent with that predicted for a resolved virtual photon with parton density functions evolving with Q^2 according to QCD motivated models. In the next section we therefore proceed to extract an effective parton density for virtual photons from the data.

6 The effective parton density for virtual photons

In order to measure the parton densities of the virtual photons we adapt the Single Effective Subprocess Approximation [12], originally developed for use in $p\overline{p}$ collisions and recently used to investigate real photon structure [13]. In LO, the cross section for the production of dijets by resolved virtual photons can be written as:

$$\frac{\mathrm{d}^5\sigma}{\mathrm{d}y\,\mathrm{d}x_\gamma\,\mathrm{d}x_\mathrm{p}\,\mathrm{d}\cos\theta^*\,\mathrm{d}Q^2} = \frac{1}{32\pi s_\mathrm{ep}} \sum_{k=T,L} \frac{f^k_{\gamma/\mathrm{e}}(y,Q^2)}{y} \sum_{ij} \frac{f^k_{i/\gamma}(x_\gamma,P_t^2,Q^2)}{x_\gamma} \frac{f_{j/\mathrm{p}}(x_\mathrm{p},P_t^2)}{x_\mathrm{p}} |M_{ij}(\cos\theta^*)|^2 . \quad (12)$$

Here the $f^T_{i/\gamma}$, $f^L_{i/\gamma}$ and $f_{i/\mathrm{p}}$ are densities of parton species i in transverse photons, longitudinal photons and the proton respectively. They are evaluated at the factorisation scale which we set equal to the renormalisation scale and choose to be P_t. The M_{ij} are matrix elements for $2 \to 2$ parton-parton hard scattering processes. s_ep is the square of the centre of mass energy in the ep collision. The fluxes of transverse and longitudinal photons are given by:

$$\begin{aligned} f^T_{\gamma/e}(y,Q^2) &= \frac{\alpha}{2\pi}\Big(\frac{1+(1-y)^2}{y}\frac{1}{Q^2} - \frac{2m_e^2 y}{Q^4}\Big) \\ f^L_{\gamma/e}(y,Q^2) &= \frac{\alpha}{2\pi}\frac{2(1-y)}{y}\frac{1}{Q^2}. \end{aligned} \quad (13)$$

The measured dijet cross-sections do not allow us to separate the various photon polarisation states or parton sub-processes. The contribution from longitudinal photons to the total high P_t jet production is expected to be small [5, 28, 10] when $P_t^2 \gg Q^2$ which is the case for most of the kinematic range considered here. However, in some bins $P_t^2 \sim Q^2$ so the longitudinal component cannot be neglected. To obtain a factorisable form, we first approximate equation (12) by:

$$\frac{\mathrm{d}^5\sigma}{\mathrm{d}y\;\mathrm{d}x_\gamma\;\mathrm{d}x_\mathrm{p}\;\mathrm{d}\cos\theta^*\;\mathrm{d}Q^2} \approx \frac{1}{32\pi s_{\mathrm{ep}}}\;\frac{f^T_{\gamma/\mathrm{e}}(y,Q^2)}{y}\;\sum_{ij}\;\frac{f^U_{i/\gamma}(x_\gamma,P_t^2,Q^2)}{x_\gamma}\;\frac{f_{j/\mathrm{p}}(x_\mathrm{p},P_t^2)}{x_\mathrm{p}}\;|M_{ij}(\cos\theta^*)|^2\;, \tag{14}$$

which includes only the transverse photon flux. We have defined a set of photon polarisation-averaged parton densities:

$$f^U_{i/\gamma}(x_\gamma,P_t^2,Q^2) \;\equiv\; f^T_{i/\gamma}(x_\gamma,P_t^2,Q^2) + \overline{\epsilon} f^L_{i/\gamma}(x_\gamma,P_t^2,Q^2), \tag{15}$$

where $\overline{\epsilon} \sim 1$ is the ratio of longitudinal to transverse fluxes, averaged over the y-range of the data. The extraction procedure described below uses Monte Carlo simulations which do not contain a longitudinal photon flux.

The Single Effective Subprocess (SES) approximation exploits the fact that the dominant contributions to the cross-section comes from parton-parton scattering matrix elements that have similar shapes and so differ mainly by their associated colour factors. Thus the sum over processes can be replaced by a single effective sub-process cross-section and effective parton densities for the photon and proton:

$$\frac{\mathrm{d}^5\sigma}{\mathrm{d}y\;\mathrm{d}x_\gamma\;\mathrm{d}x_\mathrm{p}\;\mathrm{d}\cos\theta^*\;\mathrm{d}Q^2} \approx \frac{1}{32\pi s_{\mathrm{ep}}}\;\frac{f^T_{\gamma/\mathrm{e}}(y,Q^2)}{y}\;\frac{\tilde{f}_\gamma(x_\gamma,P_t^2,Q^2)}{x_\gamma}\;\frac{\tilde{f}_\mathrm{p}(x_\mathrm{p},P_t^2)}{x_\mathrm{p}}\;|M_{\mathrm{SES}}(\cos\theta^*)|^2\;. \tag{16}$$

where the effective parton densities are

$$\tilde{f}_\gamma(x_\gamma,P_t^2,Q^2) \;\equiv\; \sum_{\mathrm{n_f}}\left(f^U_{\mathrm{q}/\gamma}(x_\gamma,P_t^2,Q^2) + f^U_{\overline{\mathrm{q}}/\gamma}(x_\gamma,P_t^2,Q^2)\right) + \frac{9}{4}\,f^U_{\mathrm{g}/\gamma}(x_\gamma,P_t^2,Q^2) \tag{17}$$

$$\text{and}\quad \tilde{f}_\mathrm{p}(x_\mathrm{p},P_t^2) \;\equiv\; \sum_{\mathrm{n_f}}\left(f_{\mathrm{q}/\mathrm{p}}(x_\mathrm{p},P_t^2) + f_{\overline{\mathrm{q}}/\mathrm{p}}(x_\mathrm{p},P_t^2)\right) + \frac{9}{4}\,f_{\mathrm{g}/\mathrm{p}}(x_\mathrm{p},P_t^2) \tag{18}$$

and the sums are over the quark flavours.

In order to extract the effective parton densities, the Bayesian unfolding method was applied again to correct the dijet cross section to the leading order diparton cross-section. This second unfolding corrects for hadronisation effects, the influence of multiple parton interactions and initial and final state QCD radiation. It uses correlations between $\{x_\gamma^{jets},\overline{E}_T\}$ and $\{x_\gamma,P_t\}$ obtained using the HERWIG(LO)-DG simulation. The effective parton density was then determined by comparing the di-parton cross section measured in the data with that predicted by the simulations with a known set of photon parton densities:

$$\tilde{f}_\gamma^{DATA} = \tilde{f}_\gamma^{MC} \times \frac{(\mathrm{d}^3\sigma_{ep}/\mathrm{d}Q^2\mathrm{d}\overline{E_t}^2\mathrm{d}x_\gamma^{jets})^{DATA}}{(\mathrm{d}^3\sigma_{ep}/\mathrm{d}Q^2\mathrm{d}\overline{E_t}^2\mathrm{d}x_\gamma^{jets})^{MC}} \tag{19}$$

The systematic errors associated with determination of the triple differential cross section measurement described in the previous section, were propagated through and the additional systematic errors associated with the second unfolding were added in quadrature. The most significant new systematic effects arise from the model dependencies. The latter were estimated by repeating the second unfolding varying the input parton densities, the amount of soft underlying event and the hadronisation models.

The transition from jet-based observables to parton variables is more strongly influenced by the presence of multiple parton interactions than was the case for the transition between hadron-based and measured jets. Note that with the different choice of minimum P_t and space-like shower parameter used in HERWIG(LO)-DG for this step in the analysis, a lower soft underlying event frequency is required to describe the energy flow outside the jets. In figure 5 we show the transverse energy flow per unit area in the (η, ϕ) plane outside the two highest E_t jets and in the range $-1.0 < \eta < 1.0$ as a function of Q^2. The observed decrease with increasing Q^2 is compared with predictions from HERWIG(LO)/DG with 0%, 5% and 10% soft underlying event and with RAPGAP(LO)/SAS-2D.

We varied the soft-underlying event probability in HERWIG between 0% and 10% in order to estimate the systematic uncertainty. The mean systematic error is 20% and the error is largest at low x_γ and low Q^2.

Additional model dependencies arising from the use of different parton showering and hadronisation mechanisms and different input parton densities were estimated by unfolding the data using the RAPGAP(LO)/SAS-1D, RAPGAP(LO)/SAS-2D and RAPGAP(LO)/DG models and comparing the results with HERWIG(LO)/DG. We assign a further 25% systematic error on the basis of this test. Finally, the stability of the unfolding procedure between iterations introduces a 10% uncertainty.

The extracted effective parton density is shown in figures 6, 7, and 8. Only points where $P_t^2 > Q^2$ are shown. It should be noted that in the highest $\overline{E_t}^2$, highest Q^2 bins, $Q^2 \to P_t^2$ the assumptions of factorisation involved in the definition of the effective parton density begin to break down. Other effects arising from higher twist contributions and longitudinally polarised photons are largest here. The figures show the evolution of the effective parton density in the photon both with the scale at which it is probed and with its virtuality. The data are compared with three sets of parton densities. The solid curves are the effective parton density calculated from the Drees-Godbole model using GRV-LO densities for the real photon and setting the free parameter in the suppression factor, ω, to 0.1 GeV. The dashed and dotted curves are calculated from the SAS-1D and SAS-2D parton densities, respectively. The predictions were evaluated at the mean x_γ and logarithmic mean Q^2 and P_t^2 of the ranges.

Figure 6 shows that the effective parton density is almost independent of x_γ in the region studied and is described by all three models within errors except in the largest Q^2 range where they tend to underestimate the data. As is characteristic of photon structure at $Q^2 = 0$, there is no tendency for the parton density to accumulate at low x_γ as the probing scale is increased.

In figure 7, the parton density is shown as a function of the square of the probing scale P_t^2 in ranges of x_γ and Q^2. Here, although the uncertainties in the measurement are still considerable, it can be seen that the parton density tends to *rise* with increasing P_t^2 throughout the kinematic region where it can be measured.

This scaling behaviour, characteristic of the point-like coupling of the photon, is seen here for the first time for virtual photons. The decrease of the parton density with virtuality is most clearly seen in Fig 8, where the Q^2 dependence is shown in ranges of P_t^2 and x_γ. The three parameterisations for the parton density all give a good description of the data both in the lowest x_γ range and in the lowest two Q^2 bins. They all predict a more rapid suppression as $Q^2 \to P_t^2$ than is seen in the data. It is in this region where non-leading terms, not accounted for in the models, are expected to become important.

In figure 9, the Q^2 evolution of the effective parton density is shown for $P_t^2 = 85\ \mathrm{GeV}^2$, in the upper figure for $0.35 < x_\gamma < 0.5$ and in the lower for $0.5 < x_\gamma < 0.7$. Superimposed on the same plots is photoproduction data at $P_t^2 = 112\ \mathrm{GeV}^2$ and x_γ values of 0.3 and 0.55 taken from reference [13] which we have extrapolated to the P_t^2 and x_γ values in the figures. The extrapolation was based on the GRV-LO parton densities which give a good description of the photoproduction data. The evolution is compared with that predicted by the three models described above and also with a simple ρ-pole suppression factor characteristic of a pure VMD model:

$$f_{i|\gamma}(x_\gamma, P_t^2, Q^2) \sim f_{i|\gamma}(x_\gamma, P_t^2, 0)\left(\frac{m_\rho^2}{m_\rho^2 + Q^2}\right)^2. \tag{20}$$

The latter clearly underestimates the data. The logarithmic suppression predicted by the virtual photon models on the other hand gives a good description below $Q^2 \sim 20\ \mathrm{GeV}^2$. At higher Q^2 the parton densities are suppressed more slowly than the models predict.

7 Conclusions

We have measured the triple differential cross section, $\mathrm{d}^3\sigma_{ep}/\mathrm{d}Q^2\mathrm{d}\overline{E_t}^2\mathrm{d}x_\gamma^{jets}$, in dijet events for $1.6 < Q^2 < 80\ \mathrm{GeV}^2$ and $0.1 < y < 0.7$. The measured cross-section shows the x_γ^{jets}, $\overline{E_t}^2$ and Q^2 behaviour expected for processes in which a virtual photon, carrying an hadronic structure evolving according to perturbative QCD, interacts with the proton via hard parton-parton scattering. As predicted by perturbative QCD, as $Q^2 \to \overline{E_t}^2$, the photon structure reduces to a simple direct coupling to $q\overline{q}$ pairs and the dijet cross-section is well-described without invoking photon structure.

An effective, leading order, parton density of the virtual photon has been extracted in the Single Effective Subprocess approximation and its dependence on x_γ, probing scale P_t^2 and target virtuality Q^2 has been measured. The photon parton density shows the logarithmic scaling characteristic of photon structure and is seen to be suppressed with increasing Q^2 as predicted by perturbative QCD.

Acknowledgements

We are grateful to the HERA machine group whose outstanding efforts have made and continue to make this experiment possible. We thank the engineers and technicians for their work in constructing and now maintaining the H1 detector, our funding agencies for financial support, the DESY technical staff for continual assistance, and the DESY directorate for the hospitality which they extend to the non-DESY members of the collaboration.

References

[1] PLUTO Collab., Ch. Berger et al., Phys. Lett. **B142** (1984) 111;
PLUTO Collab., Ch. Berger et al., Nucl. Phys. **B281** (1987) 365;
PLUTO Collab., Ch. Berger et al., Phys. Lett. **107B** (1981) 168;
JADE Collab., W. Bartel et al., Z. Phys. **C24** (1984) 231;
TASSO Collab., M. Althoff et al., Z. Phys. **C24** (1984) 231;
TPC/2γ Collab., H. Aihara et al. Phys. Rev. Lett. **58** (1987) 97;
TPC/2γ Collab., H. Aihara et al. Z. Phys. **C34** (1987) 1;
CELLO Collab., H. J. Berend et al., contributed to the XXVth Int. Conf. on HEP, Singapore 1990, unpublished;
AMY Collab., T. Sasaki et al., Phys. Lett. **B252** (1990) 491;
OPAL Collab., R. Akers et al., Z. Phys. **C61** (1994) 199;
AMY Collab., B. J. Kim et al., Phys. Lett. **B325** (1994) 248;
TOPAZ Collab., H. Hayashii et al., Phys. Lett. **B314** (1993) 149;
ALEPH Collab., D. Buskulic et al., Phys. Lett. **B313** (1993) 509;
DELPHI Collab., P. Abreu et al., Phys. Lett. **B342** (1995) 402.

[2] ZEUS Collab., M. Derrick et al., Phys. Lett. **B322** (1994) 287;
H1 Collab., T. Ahmed et al., Nucl. Phys. **B445** (1995) 195;
H1 Collab., S. Aid et al., Z. Phys. **C70** (1996) 17;
ZEUS Collab., M. Derrick et al., Phys. Lett. **B384** (1996) 401;
ZEUS Collab., J. Breitweg et al., Eur. Phys. J. **C1** (1998) 109;
H1 Collaboration, C. Adloff et al., Eur. Phys. J. **C1** (1998) 97.

[3] T. Uematsu and T. Walsh, Phys. Lett. **B101** (1981) 263;
T. Uematsu and T. Walsh, Nucl. Phys. **B199** (1982) 93;
G. Rossi, U. California at San Diego preprint UCSD-1-P10-227 (1983);
G. Rossi, Phys. Rev. **D29** (1984) 852.

[4] PLUTO Collab., Ch. Berger et al., Phys. Lett. **B142** (1984) 119.

[5] M. Glück, E. Reya and M. Stratmann, Phys. Rev. **D54** (1996) 5515.

[6] M. Klasen, G. Kramer and B. Pötter, Eur. Phys. J. **C1** (1998) 261.

[7] D. de Florian, C. Garcia Canal and R. Sassot, Z. Phys. **C75** (1997) 265.

[8] J. Chýla, J. Cvach, Proceedings of the Workshop 1995/96 on "Future Physics at HERA", eds. G. Ingelman, A. de Roeck and R. Klanner, DESY 1996, Vol. 1, 545.

[9] M. Drees and R. Godbole, Phys. Rev. **D50** (1994) 3124.

[10] F. Borzumati and G. Schuler, Z. Phys. **C58** (1993) 139.

[11] H1 Collaboration, C. Adloff et al., Phys. Lett. **B415** (1997) 418.

[12] B. V. Combridge, C. J. Maxwell, Nucl. Phys. **B239** (1984) 429.

[13] H1 Collaboration, C. Adloff et. al., Eur. Phys. J. **C1** (1998) 97.

[14] H1 Collaboration, *Di-Jet Event Rates in Deep-Inelastic Scattering at HERA*, preprint DESY-98-076, submitted to Eur. Phys. J. C.

[15] S.D. Ellis, D.E. Soper, Phys. Rev. **D48** (1993) 3160;
S. Catani, Yu.L. Dokshitzer M.H. Seymour and B.R. Webber Nucl. Phys. B406 1993, 187.

[16] H1 Collaboration, I. Abt et al., Nucl. Instr. and Meth. **A386** (1997) 310 and 348.

[17] H1 SPACAL Group, R. D. Appuhn et al., Nucl. Instr. and Meth. **A386** (1997) 397.

[18] H1 Calorimeter Group, B. Andrieu et al., Nucl. Instr. and Meth. **A336** (1993) 460.

[19] H1 Calorimeter Group, B. Andrieu et al. Nucl. Instr. and Meth. **A350** (1994) 57;
H1 Calorimeter Group, B. Andrieu et al. Nucl. Instr. and Meth. **A336** (1993) 499.

[20] G. Marchesini et al., Comp. Phys. Comm. **67** (1992) 465.

[21] H. Jung, Comp. Phys. Comm. **86** (1995) 147.

[22] G. Marchesini and B. Webber, Nucl. Phys. **B238** (1984) 1;
G. Marchesini and B. Webber, Nucl. Phys. **B310** (1988) 461.

[23] T. Sjöstrand, Comp. Phys. Comm. **82** (1994) 74;
T. Sjöstrand, CERN-TH-7112-93 (Dec. 1993, revised Aug. 1994)

[24] M. Glück, E. Reya and A. Vogt, Z. Phys. **C67** (1995) 433.

[25] M. Glück, E. Reya and A. Vogt, Phys. Rev. **D45** (1992) 3986.

[26] T. Sjöstrand and G. A. Schuler, Phys. Lett. **B376** (1996) 193.

[27] G. D'Agostini, Nucl. Instr. and Meth. **A362** (1995) 487.

[28] S. Frixione, M. Mangano, P. Nason and G. Ridolfi, Phys. Lett.**B319** (1993) 339.

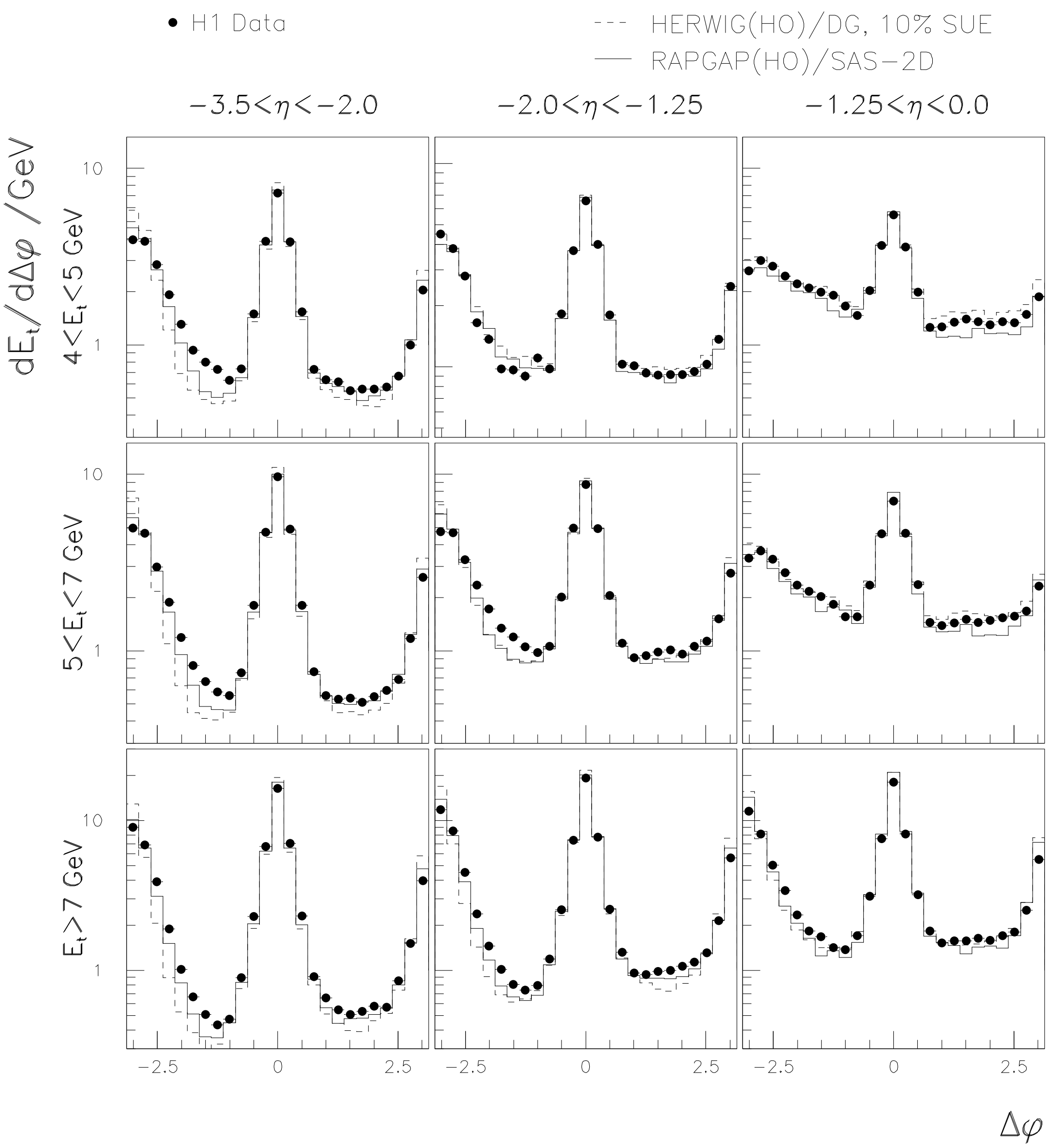

Figure 1: The observed transverse energy flow in ϕ with respect to the axes of the two highest E_t jets in the selected event sample for a slice $\mid \eta - \eta^{jet} \mid < 1$. The result is shown for various ranges of η and E_t of the jets. The second jet is always chosen to have $\phi < 0$, leaving the pedestal level clearly visible to the right of the jet core, in the region $\phi > 0$. The data are compared with predictions from the HERWIG(HO)/DG simulation with 10% soft underlying event (dashed histogram) and with the RAPGAP(HO)/SAS-2D model.

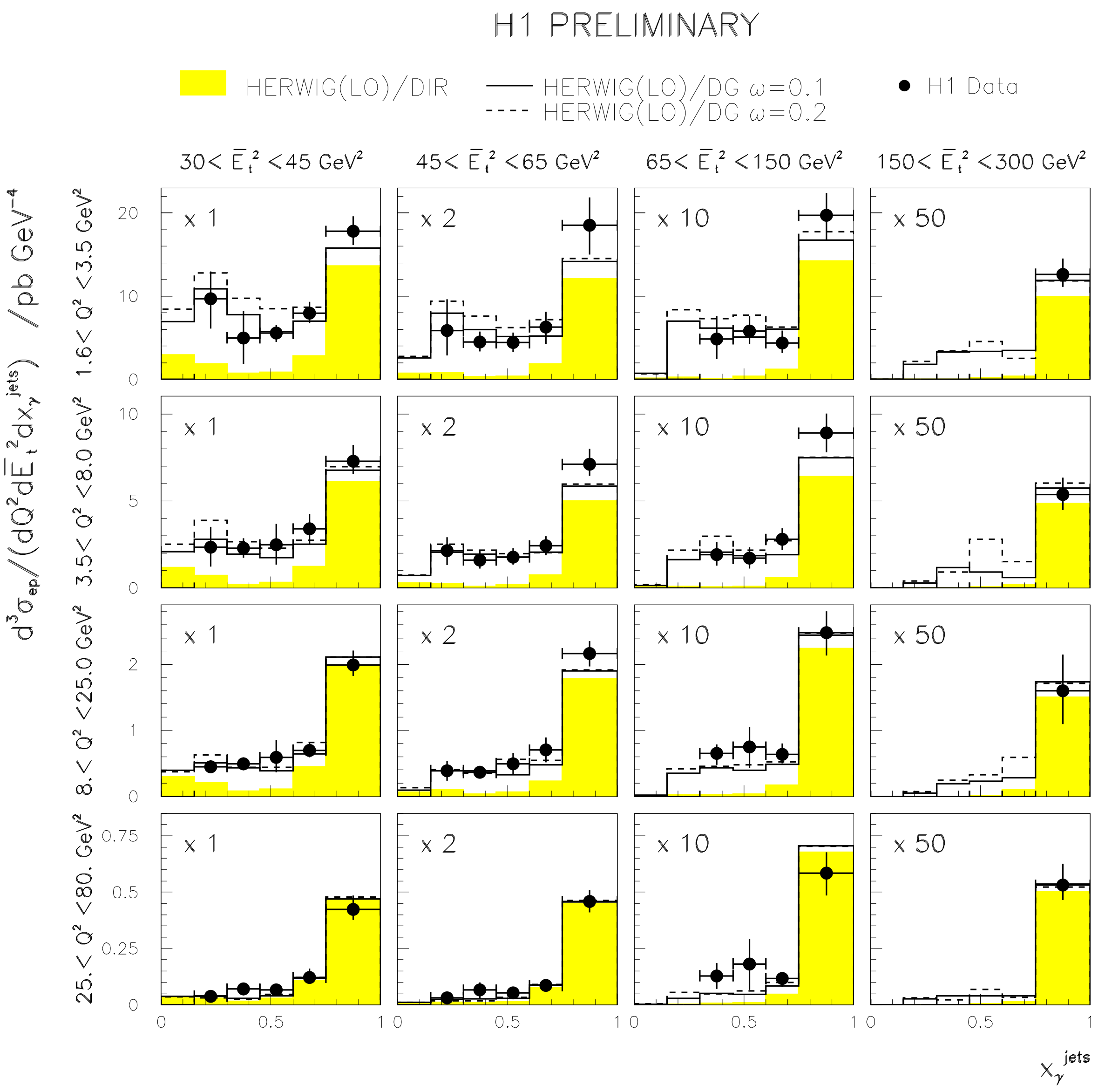

Figure 2: The differential dijet cross-section $\mathrm{d}^3\sigma_{ep}/\mathrm{d}Q^2\mathrm{d}\overline{E_t}^2\mathrm{d}x_\gamma^{jets}$ shown as a function of x_γ^{jets} for different regions of $\overline{E_t}^2$ and Q^2. The scale factors applied to the cross-sections are indicated. The data (points) are corrected for detector effects and the error bar shows the quadratic sum of systematic and statistical errors. Also shown is the HERWIG(LO)/DG model with 10% soft-underlying event and two choices of the Q^2 suppression factor ω. The full histogram is for $\omega = 0.1$ and the dashed for $\omega = 0.2$. The direct component of this model is shown as the shaded histogram.

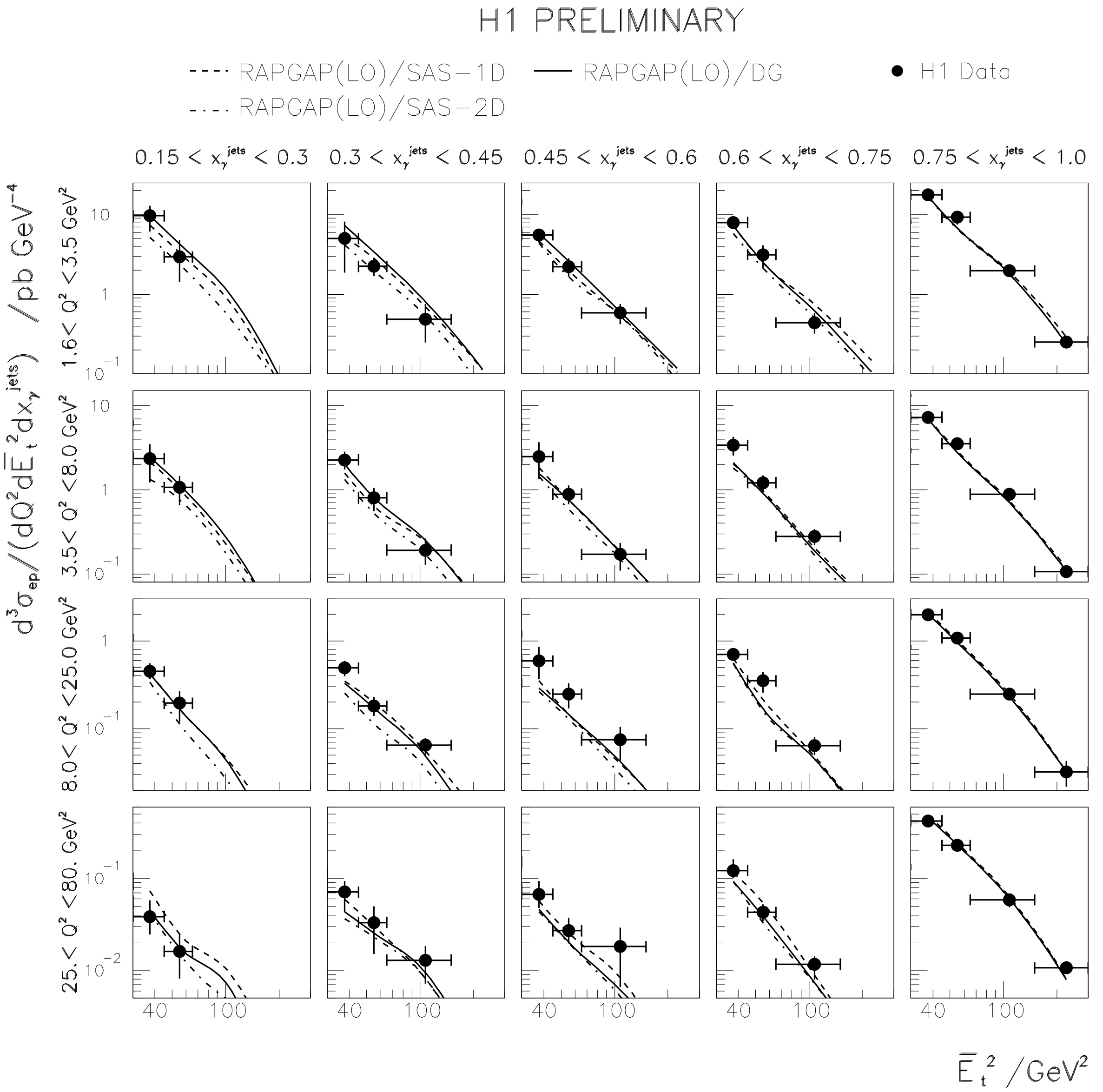

Figure 3: The differential dijet cross-section $\mathrm{d}^3\sigma_{ep}/\mathrm{d}Q^2\mathrm{d}\overline{E_t}^2\mathrm{d}x_\gamma^{jets}$ shown as a function of $\overline{E_t}^2$ for different regions of x_γ^{jets} and Q^2. The data (points) are corrected for detector effects and the error bar shows the quadratic sum of systematic and statistical errors. Also shown is the RAPGAP(LO) model with three choices of photon parton density. The DG model with GRV-LO real photon densities and $\omega = 0.2$ is shown as the full curve. The predictions with SAS-1D and SAS-2D are shown as the dashed and dot-dashed curves respectively.

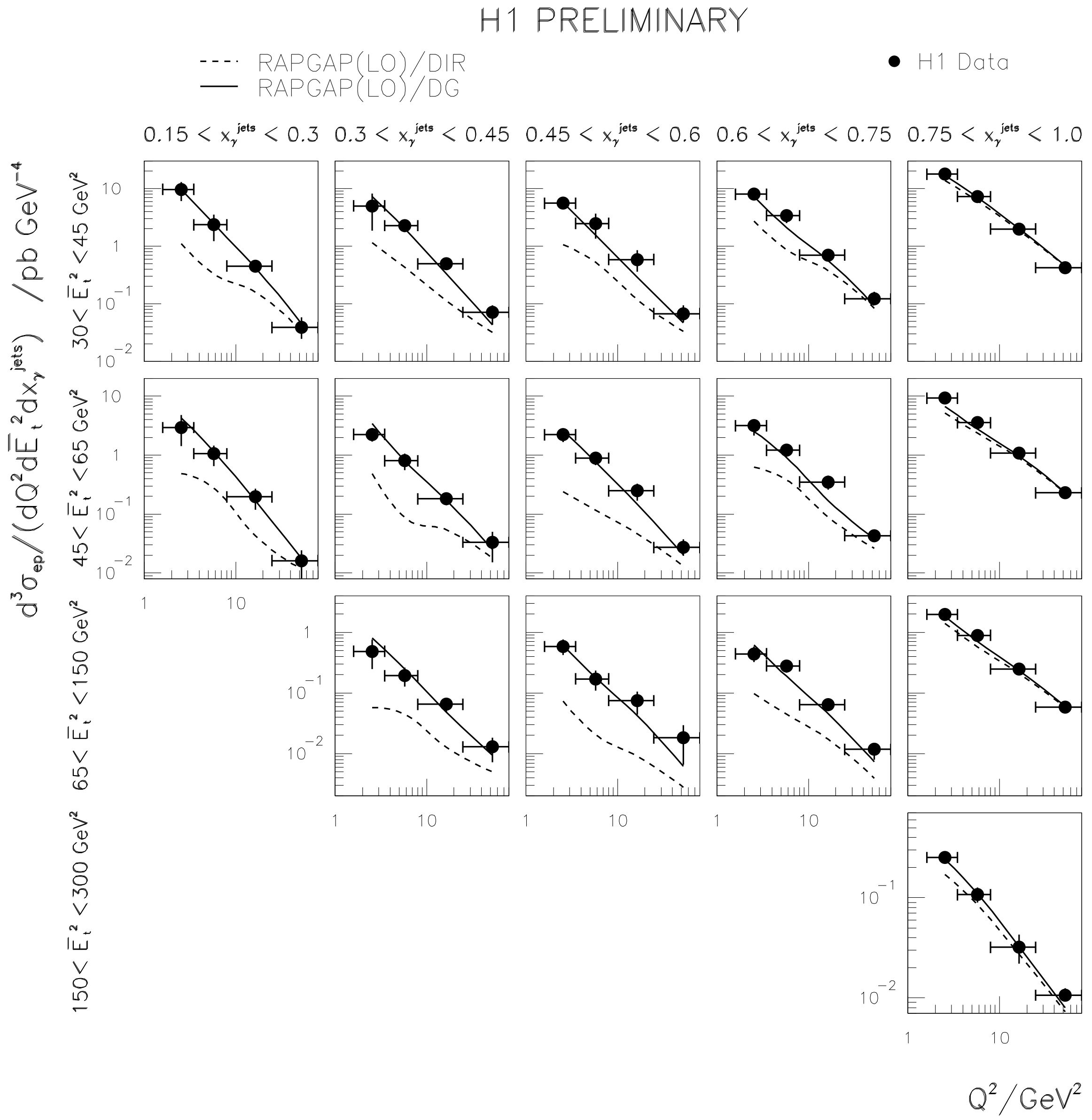

Figure 4: The differential dijet cross-section $\mathrm{d}^3\sigma_{ep}/\mathrm{d}Q^2\mathrm{d}\overline{E_t}^2\mathrm{d}x_\gamma^{jets}$ shown as a function of Q^2 for different regions of x_γ^{jets} and $\overline{E_t}^2$. The data (points) are corrected for detector effects and the error bar shows the quadratic sum of systematic and statistical errors. Also shown is the prediction from the RAPGAP(LO)/DG model, shown as the full curve. The dashed curve shows the prediction for the direct photon processes in this model.

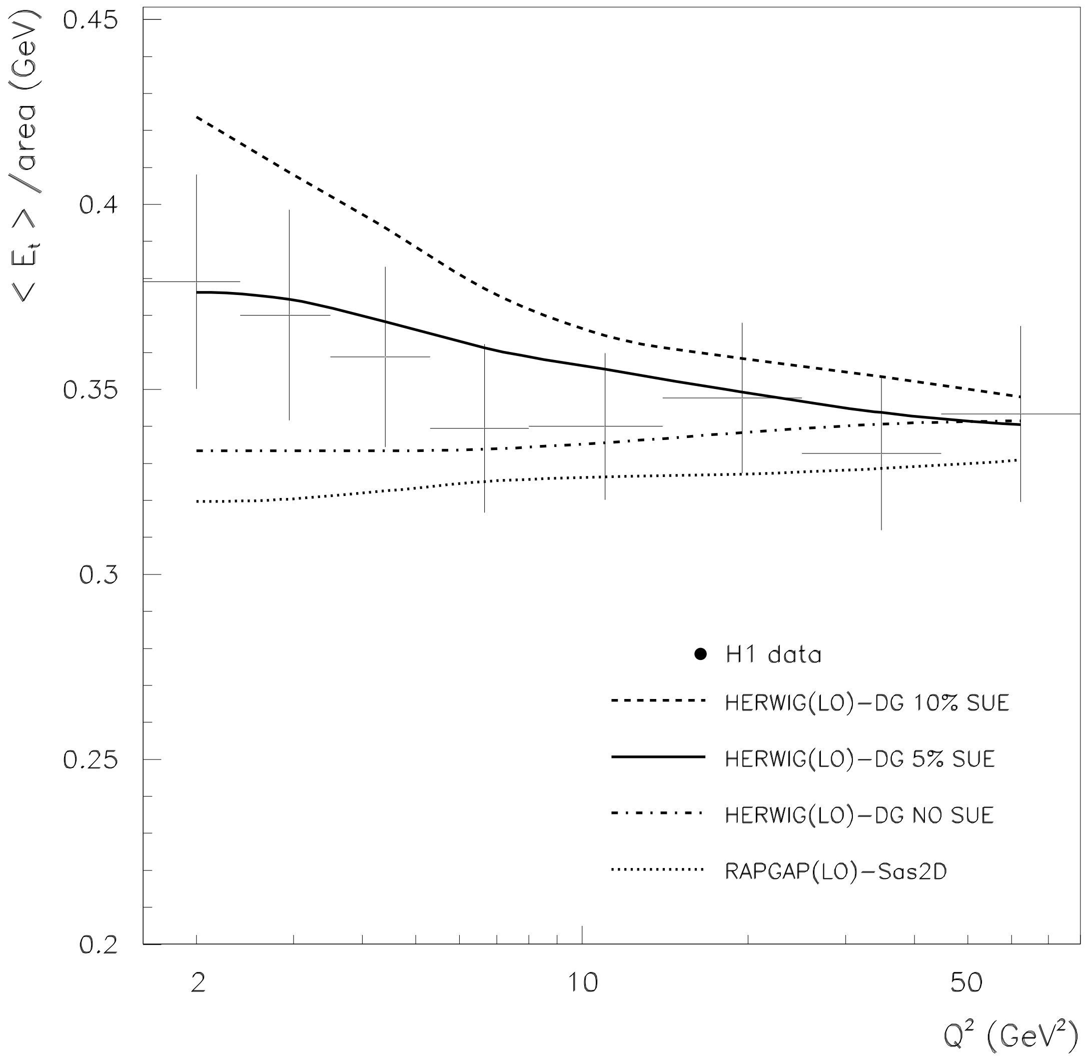

Figure 5: The average transverse energy per unit area in $\eta - \phi$ space outside the two highest E_T jets and in the range $-1.0 < \eta < 1.0$ in the $\gamma^* p$ cms as a function of Q^2. The data are corrected for detector effects. The errors are statistical only. Also shown is the prediction from the HERWIG(LO)/DG model with three choices for the percentage of resolved events with a soft underlying event: 0% (dash-dotted), 5% (full) and 10% (dashed). The prediction from the RAPGAP(LO)/SAS-2D model is shown as the dotted curve.

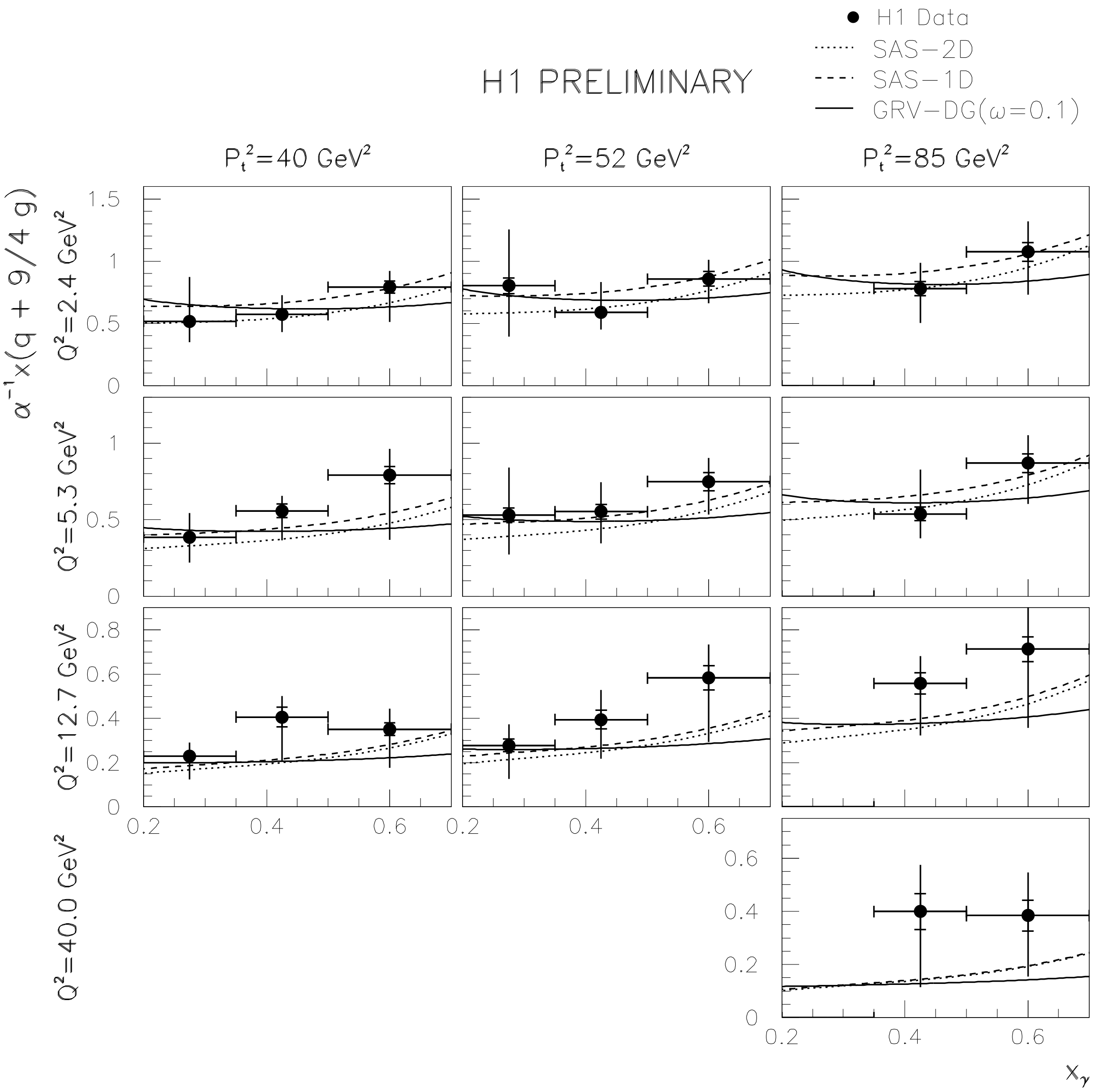

Figure 6: The leading order effective parton density of the photon $x(q + 9/4g)$, divided by the fine structure constant α, as a function of x_γ for different values of Q^2 and P_t^2. The data are displayed as points, with the inner error bar depicting the statistical error, and the total error bar the quadratic sum of statistical and systematic errors. Also shown are the prediction from the DG model using GRV-LO real photon parton densities and $\omega = 0.1$ (solid line) and the SAS-1D (dashed line) and SAS-2D(dot-dashed line) parameterisations.

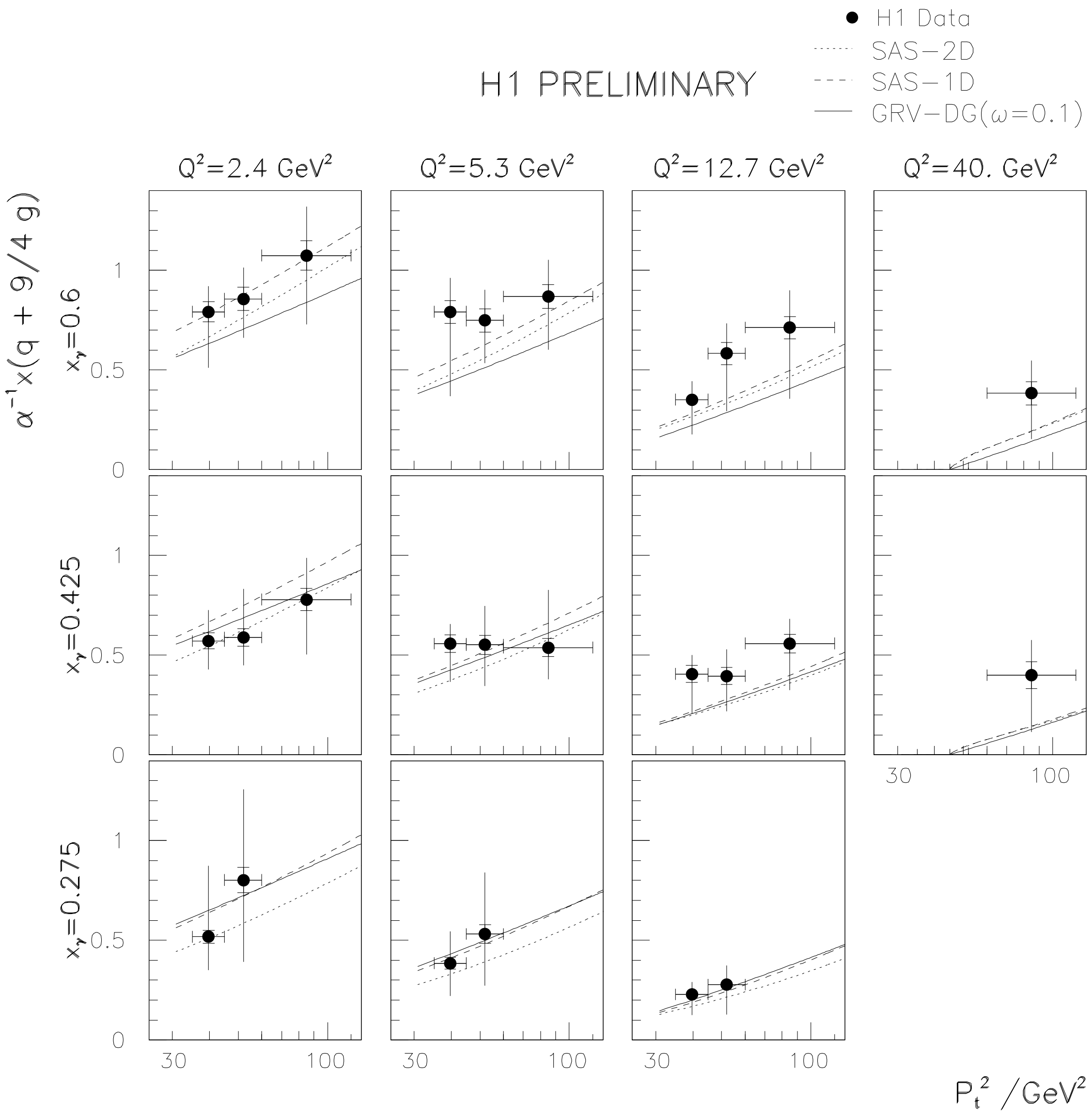

Figure 7: The leading order effective parton density of the photon $x(q + 9/4g)$, divided by the fine structure constant α, as a function of the squared parton tranverse momentum, P_t^2, for different values of Q^2 and x_γ. The data are displayed as points, with the inner error bar depicting the statistical error, and the total error bar the quadratic sum of statistical and systematic errors. Also shown are the prediction from the DG model using GRV-LO real photon parton densities and $\omega = 0.1$ (solid line) and the SAS-1D (dashed line) and SAS-2D(dot-dashed line) parameterisations.

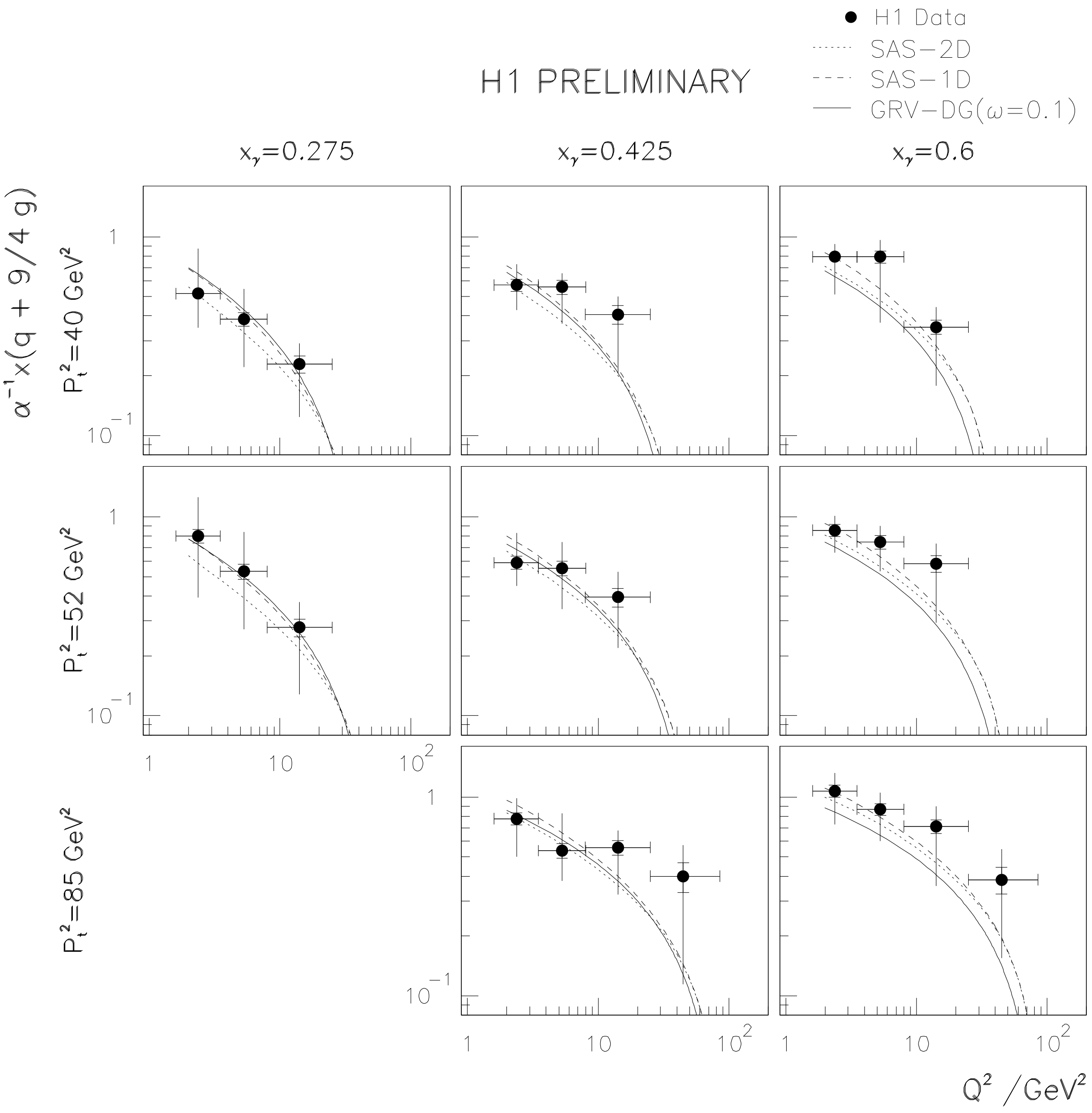

Figure 8: The leading order effective parton density of the photon $x(q + 9/4g)$, divided by the fine structure constant α, as a function of Q^2 for different values of P_t^2 and x_γ. The data are displayed as points, with the inner error bar depicting the statistical error, and the total error bar the quadratic sum of statistical and systematic errors. Also shown are the prediction from the DG model using GRV-LO real photon parton densities and $\omega = 0.1$ (solid line) and the SAS-1D (dashed line) and SAS-2D (dot-dashed line) parameterisations.

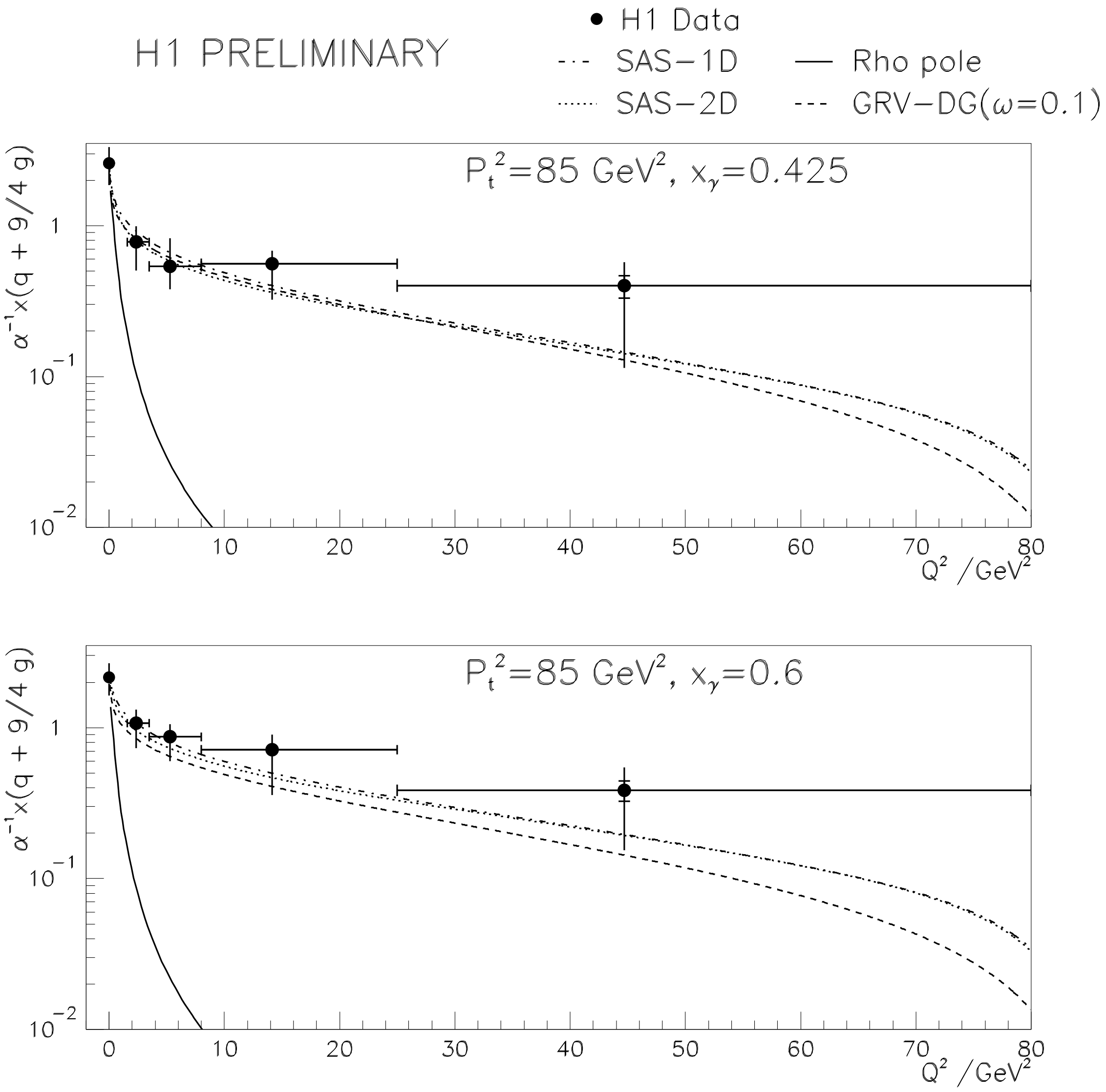

Figure 9: The leading order effective parton density of the photon $x(q + 9/4g)$, divided by the fine structure constant α, as a function of Q^2 for $P_t^2 = 85\mathrm{GeV}^2$ and two values of x_γ. The data are displayed as points, with the inner error bar depicting the statistical error, and the total error bar the quadratic sum of statistical and systematic errors. The points at $Q^2 = 0$ are taken from reference [13] scaled by factors derived from GRV-LO parton densities. Also shown are the prediction from the DG model using GRV-LO real photon parton densities and $\omega = 0.1$ (solid line) and the SAS-1D (dashed line) and SAS-2D(dot-dashed line) parameterisations. The solid curve shows the photoproduction data scaled by a ρ-pole factor (see text)